

Handheld spatial frequency domain imager for noninvasive Sjögren's syndrome labial salivary gland biopsy

**BIXIN ZENG,^{1,4,5} MINGROU GUO,^{1,4} KANGYUAN YU,¹ LI SUN,²
WEIHAO LIN,¹ DA PAN,¹ XIAOWEI CHEN,² AND MIN XU^{1,3,6} **

¹*Institute of Lasers and Biomedical Photonics, Biomedical Engineering College, Wenzhou Medical University, Wenzhou, Zhejiang, 325035, China*

²*The First Affiliated Hospital of Wenzhou Medical University, Wenzhou, Zhejiang, 325035, China*

³*Department of Physics and Astronomy, Hunter College and the Graduate Center, The City University of New York, 695 Park Avenue, New York, NY 10065, USA*

⁴*These authors contributed equally.*

⁵*929467139@qq.com*

⁶*minxu@hunter.cuny.edu*

Abstract: A labial salivary gland biopsy (LSGB) plays an essential role in diagnosing Sjögren's syndrome (SS), but its clinical application is limited due to its invasiveness. Here, we present a handheld single snapshot multiple-frequency demodulation-spatial frequency domain imaging (SSMD-SFDI) device for a rapid optical biopsy of labial salivary glands noninvasively. The structural and physiological parameters of lower lip mucosa were obtained from the light reflectance of the layered oral mucosa. The recovered parameters were found to correlate strongly with the progression of SS. In our pilot study on 15 healthy subjects and 183 SS patients, a support vector machine (SVM) classifier using the measured parameters distinguished healthy subjects, LSGB I, II, III, and IV patients in sequence with AUCs of 0.979, 0.898, 0.906, and 0.978, respectively. Critical structural and physiological alterations in the mucosa due to SS were further identified and used to assess its risk using an explainable neural network. The handheld spatial frequency domain imager may serve as a valuable label-free and noninvasive tool for early diagnosing and surveying SS.

© 2021 Optical Society of America under the terms of the [OSA Open Access Publishing Agreement](#)

1. Introduction

Sjögren's syndrome (SS) is a chronic inflammatory autoimmune disease mainly involving exocrine glands [1,2]. The clinical manifestations of the disease are diverse, and the pathogenesis remains obscure. In addition to the symptoms of dry mouth and dry eyes caused by damaged salivary glands and lacrimal glands [3], other exocrine glands and organs may suffer multisystem disorder as well. For example, the skin, joints, kidneys, lungs, digestive system, nerves, and hematological system are affected to varying degrees [4,5].

SS is a serious condition and cannot be completely cured at present. Timely treatment of SS is critical such that complications are less likely to develop. Once treated in time, individuals can usually manage the condition well. Therefore, early detection and surveillance are particularly important for the control of this disease.

Diagnostic criteria of SS were published by the American–European Consensus Group (AECG) in 2002 and the American College of Rheumatology (ACR) in 2012 [6,7]. The diagnosis of SS lacks a definite gold standard and requires comprehensive analysis. The main objective diagnostic criteria include histopathological examination (labial salivary gland biopsy (LSGB)), serological examination (anti-SSA/Ro antibody positivity), unstimulated whole salivary flow rate test, Schirmer's test, and corneal staining test. The new classification standard for primary SS

recommended by the ACR/EULAR in 2016 [8] uses a sum of scores for different classification criteria, among which the weight of LSGB and anti-SSA/Ro antibody positivity is the highest. Alternative diagnostic methods such as parotid gland scintigraphy, parotid ultrasound, and magnetic resonance have also emerged, but these methods have not yet been fully recognized in the clinic [9]. LSGB and blood marker-antibody positive method have high specificity and sensitivity [10–12]. However, none of these methods alone can be used as the gold standard for diagnosing SS, and the diagnosis process is invasive and time-consuming. LSGB even requires traumatic surgery, which can cause psychological panic and physical injury to the patient.

In this work, we first present a handheld Single Snapshot Multiple-frequency Demodulation-Spatial Frequency Domain Imaging (SSMD-SFDI) imager for label-free and noninvasive LSGB. The SSMD-SFDI imager maps the structural and hemodynamic properties of the layered oral mucosa in realtime. We then report a pilot study on a cohort of healthy subjects ($n = 15$) and patients with different pathological grades of LSGB ($n = 183$, 46 LSGB I, 39 LSGB II, 48 LSGB III, 50 LSGB IV) with the SSMD-SFDI imager. The recovered structural and physiological parameters are found to correlate significantly with the progression of SS. Both diagnosis and risk stratification of SS based on the measurement by the SSMD-SFDI imager is then demonstrated. This imager provides a valuable label-free and noninvasive solution for early diagnosis, routine surveillance, and therapy efficacy monitoring of SS.

2. Methods and materials

2.1. SSMD-SFDI imager

SFDI is an emerging modality with the potential for non-contact, rapid evaluation of the optical properties of turbid media (such as biological tissues) over a large field of view. It quantifies the sample optical properties from the modulation transfer function (MTF) of the light reflectance with structured light.

The SSMD-SFDI method detailed in our previous studies [13–15] requires a single snapshot and extracts multiple AC and DC components from a structured light reflectance image simultaneously. Briefly, the structured light pattern incident on the sample surface and the light intensity pattern backscattered by the sample can be expressed as:

$$I_0(x, y) = I_{DC}^{(0)} + \sum_{i=1}^k I_{AC,i}^{(0)} \cos[2\pi(f_{x,i}x + f_{y,i}y) + \phi_i] \quad (1)$$

$$I(x, y) = I_{DC}(x, y) + \sum_{i=1}^k I_{AC,i}(x, y) \cos[2\pi(f_{x,i}x + f_{y,i}y) + \phi_i] \quad (2)$$

where $k \geq 1$ is the number of AC components, $I_{AC,i}^{(0)}$ and $I_{AC,i}$ are the incident amplitude and backscattering amplitude of the i -th AC component of spatial frequency $(f_{x,i}, f_{y,i})$ and phase ϕ_i , respectively. $I_{AC,i}$, I_{DC} can be obtained by demodulation as:

$$I_{AC,i} = \frac{\sqrt{\left[\iint_{\sigma} I(x, y) \cos(2\pi f_{x,i}x + 2\pi f_{y,i}y) dx dy\right]^2 + \left[\iint_{\sigma} I(x, y) \sin(2\pi f_{x,i}x + 2\pi f_{y,i}y) dx dy\right]^2}}{\iint_{\sigma} \cos^2(2\pi f_{x,i}x + 2\pi f_{y,i}y) dx dy} \quad (3)$$

$$I_{DC} = \frac{1}{T_1 \times T_2} \iint_{\sigma} I(x, y) dx dy \quad (4)$$

where σ represents the kernel window of an appropriate size $T_1 \times T_2$. MTF is given by:

$$\text{MTF}_{AC} = \frac{I_{AC,i}}{I_{AC,i}^{(0)}}, \text{MTF}_{DC} = \frac{I_{DC}}{I_{DC}^{(0)}}. \quad (5)$$

The optical properties (absorption and scattering) of the sample are then recovered from the MTFs based on a reflectance model of spatially modulated light [14,16,17]. Among various demodulation methods for SFDI, SSMD has several unique features. Conventional three-phase demodulation requires three images to obtain AC and DC components, whereas SSMD demodulates multiple AC components from one single snapshot, suppressing both motion artifacts and measurement noise. In addition, compared with other single snapshot SFDI approaches, the advantage of SSMD lies in its robustness against measurement imperfection and its superiority in SNR [14]. However, when the kernel window σ is larger than the scale over which the medium's optical properties vary, SSMD may lead to a sacrifice in the spatial resolution and introduce error [14].

The handheld SSMD-SFDI imager is shown in Fig. 1. Light from an RGB LED source (GCSI-800110, Daheng Optics) passes through the collimating lens and a grating (GT-SG-TPS001, RealLight) to produce a sinusoidal fringe pattern. The structured light is then magnified by a projection objective and projected onto the sample. The backscattered light from the sample is imaged onto a CMOS camera (Point Gray Grasshopper3 GS3-U3-51S5C-C) through a thin-film beam splitter (CM1-BP145B1, Thorlabs).

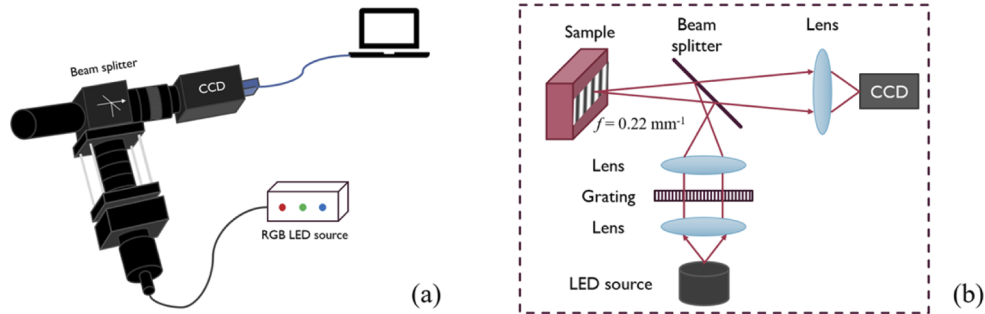


Fig. 1. (a) The handheld SSMD-SFDI imager. (b) A schematic diagram of the handheld SSMD-SFDI imager.

2.2. Imaging layered mucosa in the spatial frequency domain

Biological tissues, such as skin and cervical walls, are highly structured. We have developed a strategy for imaging layered structures in the spatial frequency domain based on layered structure mapping, accounting explicitly for the dependence of the average penetration depth on the spatial modulation frequency and the wavelength of the probing light [13,18,19]. Both the structural and physiological characteristics of each layer can be recovered using this method.

The oral mucosa inside the lower lip is divided into the epithelium and lamina propria (vascularized) [20]. The predominant chromophores in the oral mucosa are oxyhemoglobin (HbO_2) and deoxyhemoglobin (Hb). The absorption coefficient of the lamina propria can be written as:

$$\mu_{a,\text{lamina propria}}(\lambda) = \varepsilon_{\text{Hb}}(\lambda)c_{\text{Hb}} + \varepsilon_{\text{HbO}_2}(\lambda)c_{\text{HbO}_2} \quad (6)$$

where ε_{Hb} , $\varepsilon_{\text{HbO}_2}$ are the molar extinction coefficients of deoxyhemoglobin and oxyhemoglobin, c_{Hb} , c_{HbO_2} are the concentration of deoxyhemoglobin and oxyhemoglobin, and λ is the wavelength.

Mapping the two-layer structure of the oral mucosa to an equivalent homogeneous medium (see Fig. 2), the following equation regarding the absorption and scattering coefficients $\mu_a(q, \lambda)$

and $\mu'_s(q, \lambda)$ of the equivalent homogeneous medium is obtained:

$$\mu_a(q, \lambda)L(q, \lambda) = \mu_{a, \text{lamina propria}}(\lambda)(L - h) \quad (7)$$

$$\mu'_s(q, \lambda)L(q, \lambda) = \mu'_{s1}(\lambda)h + \mu'_{s2}(\lambda)(L - h) \quad (8)$$

where h is the epithelial thickness, and L is the average penetration depth of the modulated light at the spatial modulation frequency f and wavelength λ , given by

$$L(q, \lambda) = \frac{(1 + Ql)^2(2\mu'_t)^{-2} + (1 + \mu'_t l)^2(2Q)^{-2} - 2(1 + Ql)(1 + \mu'_t l)(Q + \mu'_t)^{-2}}{(1 + Ql)^2(2\mu'_t)^{-1} + (1 + \mu'_t l)^2(2Q)^{-1} - 2(1 + Ql)(1 + \mu'_t l)(Q + \mu'_t)^{-1}} \quad (9)$$

where $\mu'_t \equiv \mu_a + \mu'_s$, $Q \equiv \sqrt{q^2 + 3\mu_a(\mu_a + \mu'_s)}$, $q \equiv 2\pi f$, l is the extrapolation length of diffusive light [17].

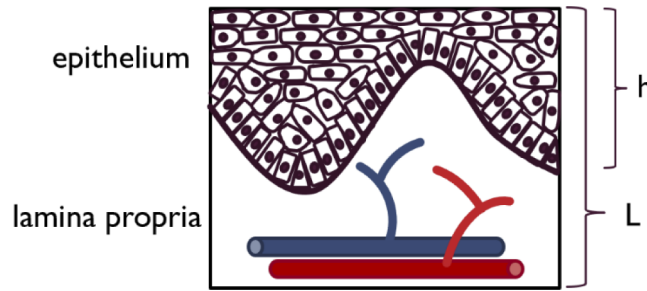


Fig. 2. The layered mucosa is mapped to an equivalent homogeneous medium of absorption coefficient $\mu_a(q, \lambda)$ and reduced scattering coefficient $\mu'_s(q, \lambda)$.

The scattering coefficients μ'_{s1} and μ'_{s2} of the epithelium and lamina propria, respectively, are assumed to follow a power law:

$$\mu'_{s1}(\lambda) = \mu'_{s1}(\lambda_0)(\lambda/\lambda_0)^{-sp_1} \quad (10)$$

$$\mu'_{s2}(\lambda) = \mu'_{s2}(\lambda_0)(\lambda/\lambda_0)^{-sp_2} \quad (11)$$

where sp_1 and sp_2 represent the scattering power of the epithelium and lamina propria, respectively [21–24]. λ_0 is set to 519 nm in this study. The efficacy of the mapping strategy is addressed in our previous studies [13].

2.3. Experimental procedure and data analysis

The study protocol was approved by the First Affiliated Hospital of Wenzhou Medical University Institutional Review Board (IRB). The SSMD-SFDI imager was used to image the oral mucosa of the lower lip of subjects. The cohort (see Table 1) included healthy subjects ($n = 15$) and patients with different pathological grades of LSGB ($n = 183$, 46 LSGB I, 39 LSGB II, 48 LSGB III, 50 LSGB IV). The single snapshot acquisition included three wavelengths (629 nm, 519 nm, and 453 nm), which provide high sensitivity to separate deoxy- and oxyhemoglobin in the oral mucosa [13]. The measured light intensities in the R, G, B channels are corrected to remove the overlap between the spectral response of the color camera [13]. The exposure time of the CCD camera is 100ms. The spatial frequencies of $f = 0 \text{ mm}^{-1}$ and $f = 0.22 \text{ mm}^{-1}$ are used in this study. The field of view of the imaged region is a circular area with a diameter of 22 mm. The imaging window is positioned to avoid the area of oral ulcers and damaged oral mucosa to mitigate the potential confounding effects of wound-healing or wound presence. We also avoid glare-reflection regions caused by saliva for the demodulation area. A region of interest (ROI) of

size 1.89mm x 1.89mm at the center of the image window was selected for data analysis. The acquisition time of a picture is 100ms. Multiple measurements were taken for each subject from different areas. Six images per subject are typically taken. The total acquisition time is about 30 seconds.

Table 1. Subjects

Subject	n	ROIs
Healthy	15	107
LSGB I	46	262
LSGB II	39	198
LSGB III	48	221
LSGB IV	50	260
Total	198	1048

Figure 3 shows a typical measurement for a healthy subject. The blue rectangle outlines the area used for demodulation by SSMD to extract the AC and DC components and compute the MTFs. The structural and physiological parameters of the epithelium and lamina propria were then recovered based on layered structure mapping for SFDI, including epithelial reduced scattering coefficient (μ'_{s1}), epithelial scattering power (sp_1), lamina propria reduced scattering coefficient (μ'_{s2}), lamina propria scattering power (sp_2), epithelial thickness (h), Alpha (surface roughness), the oral mucosa hemoglobin concentration (THb), and oxygen saturation (StO_2). The

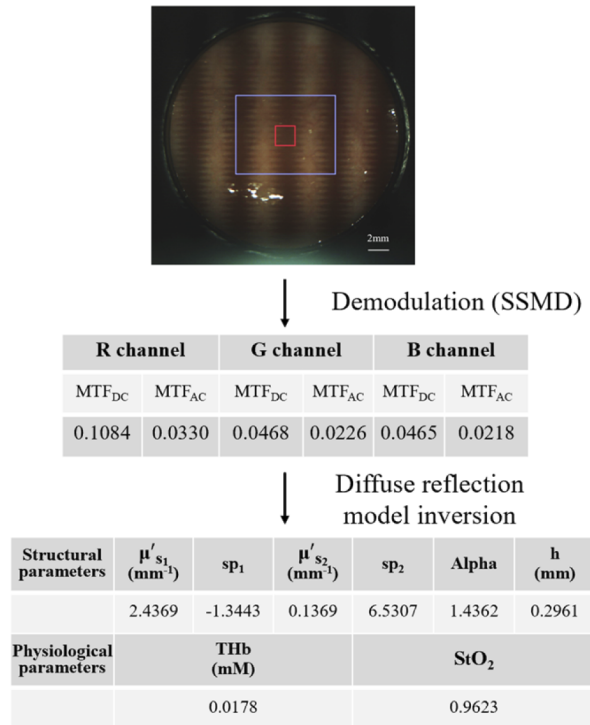


Fig. 3. A typical structured reflectance image recorded for oral mucosa of a healthy subject. The blue rectangle outlines the demodulation area, and the red square outlines the ROI within the image window used for data analysis.

structural parameters are reported for $\lambda_0 = 519$ nm. The properties of the two-layer oral mucosa are then fitted using the function `fmincon` in MATLAB by minimizing the least squared error:

$$\text{error} = \sum_{i=1}^3 [(MTF_{AC}(\lambda_i) - mtf_{AC}(\lambda_i))^2 + (MTF_{DC}(\lambda_i) - mtf_{DC}(\lambda_i))^2] \quad (12)$$

where $i = 1, 2, 3$ represent the three colors, and the theoretical values of the modulation transfer functions `mtfs` are computed with the enhanced diffusion model for the equivalent homogeneous medium [16,17]. The upper and lower limits of parameter fitting are determined by their physiological range. We accept the fitting result only if `fmincon` returns with a success flag and a low fitting error ($< 10^{-7}$).

We then use a support vector machine (SVM) to classify healthy subjects, LSGB I, II, III, and IV SS patients based on the structural and physiological parameters. Critical structural and physiological alterations in the mucosa due to SS were identified and used to assess SS risk using an explainable neural network GAMI-Net.

3. Results

3.1. Histopathology of LSGB

All patients with suspected SS in this study underwent LSGB immediately after SSMD-SFDI imaging. The standard procedure for LSGB was followed. At least four gland lobules are selected for pathological examination for lymphocyte infiltration and clustered plasma cells. The pathological examination results of the LSGB adopt Chisholm and Mason classification standard [25], and the pathological grade is divided into I, II, III, IV (see Table 2). Figure 4 shows representative histopathological images for subjects of four different pathological grades in this study.

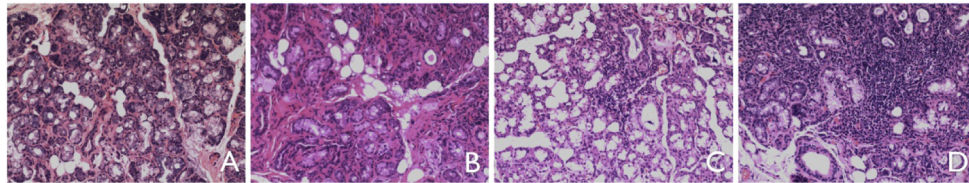


Fig. 4. Representative histopathological images for LSGB (A) I, (B) II, (C) III, and (D) IV subjects.

Table 2. Classification of Pathological Grade of LSGB According to Chisholm and Mason Classification Standards

Grade	Acinus	Glandular duct	Interstitial lymphocyte infiltration	Clinical significance
I	Normal structure	Normal structure	Slight infiltrate	meaningless
II	Occasionally acinar atrophy	Duct is not dilated	Moderate infiltrate or less than one focus ^a	suspicious
III	A small portion of acinar atrophy	Intralobular catheter dilation	One focus	positive
IV	Acinar atrophy > 1/3	Intralobular catheter dilation	More than one focus	positive

^aFocus = an aggregate of 50 or more lymphocytes and histiocytes in 4 mm².

3.2. SSMD-SFDI measured parameters and disease progression

SS is a multisystem autoimmune disease characterized by systemic multi-organ manifestations. Figure 5 summarizes that the measured parameters for SS patients are significantly different from those for healthy subjects. The clinical features of SS in the blood system are mainly manifested as cytopenia. Recent studies have shown that some SS patients have anemia,

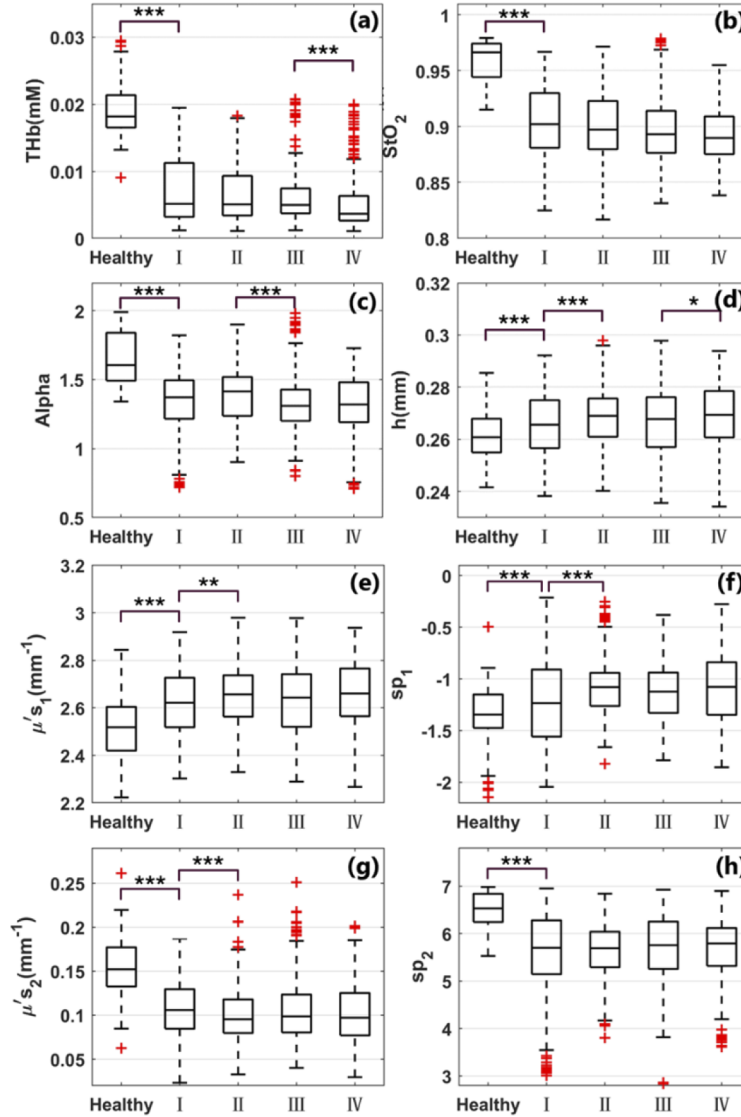


Fig. 5. Box plot graph shows the distribution of physiological parameters (THb, StO₂) and structural parameters (Alpha, h, $\mu's_1$, sp₁, $\mu's_2$, sp₂) of five groups (healthy subjects, patients with LSGB I, II, III, and IV). The horizontal line in each box is a median (50th percentile) of the measured values; the top and bottom of the boxes represent the 25th and 75th percentiles, respectively; and whiskers indicate the range from the largest to smallest observed data points within a 1.5-interquartile range presented by the box. Statistical analysis was performed using *Mann-Whitney U-test*. The significance is presented by “*” ($p < 0.05$), “**” ($p < 0.01$), and “***” ($p < 0.001$).

leukopenia, and thrombocytopenia [26], and a fall in hemoglobin and hematocrit was observed [27]. Low hematocrit means the insufficient oxygen-carrying capacity of the blood. Moreover, the complications of SS in the lungs result in interstitial lesions. A small number of SS patients have pulmonary hypertension and pulmonary fibrosis [28]. Such complications will cause the oxygen-carrying capacity of hemoglobin to decrease, thereby affecting local microcirculation. As can be seen from panels (a) and (b) of Fig. 5, when the pathological grade of LSGB increases, the hemoglobin concentration and oxygen saturation in oral mucosa show a decreasing trend.

The most common symptoms of SS are dry eyes and dry mouth. Salivary gland disease reduces the saliva secreted by the patient [29], and the surface of the oral mucosa appears dry. The decreasing trend of Alpha is consistent with the fact that the oral mucosa surface becomes rougher with SS (see Fig. 5(c)). Oral mucosal atrophy, fungal infection, and inflammatory cell infiltration can cause hyperplasia. The observed range and slight increase of the epithelial thickness (see Fig. 5(d)) in SS patients agree well with earlier OCT studies [30–32].

The reduced scattering coefficient and scattering power of the epithelium showed an upward trend (see Fig. 5(e), 5(f)), and the reduced scattering coefficient and scattering power of the lamina propria showed a downward trend (see Fig. 5(g), 5(h)). The former can be attributed to the structural alterations in oral mucosal epithelial cells that both the nucleus-cytoplasm ratio of epithelial cells and the number of cells per unit area in SS patients increase comparing to healthy subjects [33]. The rising nucleus to cytoplasm ratio results in an elevated contribution from larger scatterers accompanied by the increasing scattering power [21,22,24]. The tighter spacing between the cells leads to a larger reduced scattering coefficient of the epithelium. The latter can be attributed to atrophy of the glands, dilation of the catheter, and dilation of the capillaries in the lamina propria [34].

3.3. SVM classification

We use a classifier trained by SVM to classify healthy subjects, LSGB I, II, III, and IV SS patients using libsvm [35]. The data ($n = 1048$) was split 7:3 randomly into a training set and a test set. The features used in training include physiological parameters (THb, StO₂) and structural parameters (Alpha, h , μ'_{s1} , sp_1 , μ'_{s2} , sp_2). The classifiers are kernel-based SVM with the radial basis function (RBF) as the kernel function. Different weights were assigned to the positive and negative instances to account for data imbalance. An SVM scheme of nested 5-fold cross-validation was used to suppress any potential biases and account for the imbalanced data of a limited sample size explicitly [36]. Four binary classifications were then conducted in sequence to classify the cohort of subjects into healthy subjects, patients with LSGB I, II, III, and IV, respectively, as outlined in Fig. 6.

The Receiver Operating Characteristic (ROC) curves generated from the test data sets for the four successive binary classifications were shown in Fig. 7–10. ROC curves were computed by varying the threshold to interpret the true positive rate and the false positive rate of the predictions. The optimal thresholds for the four ROC curves are 0.949, 0.647, 0.780, and 0.662, respectively, yielding sensitivities 94.3%, 87.0%, 89.5%, and 92.7% and specificities 97.2%, 80.9%, 80.4%, and 95.2% for the four classifiers. The area under the ROC curve (AUC) for the four binary classifications is computed to be 0.979, 0.898, 0.906, and 0.978. AUCs on both the training and test data sets for the four classifiers in each fold of cross-validation are listed in Table 3.

3.4. Risk factors

Critical structural and physiological alterations in the mucosa due to SS were identified and used to assess SS risk using an explainable neural network GAMI-Net. GAMI-Net, based on generalized additive models with structured interactions, has superior interpretability while maintaining competitive prediction accuracy [37]. Through GAMI-Net analysis, we extracted leading main and pairwise interaction effects and estimated their contributions to the overall risk.

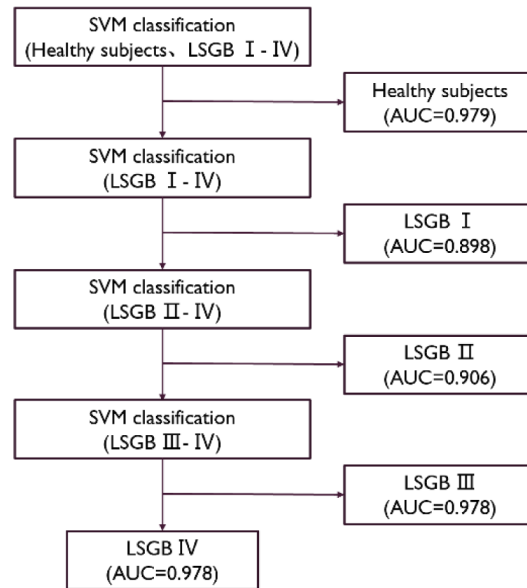


Fig. 6. Diagram of classification by SVM.

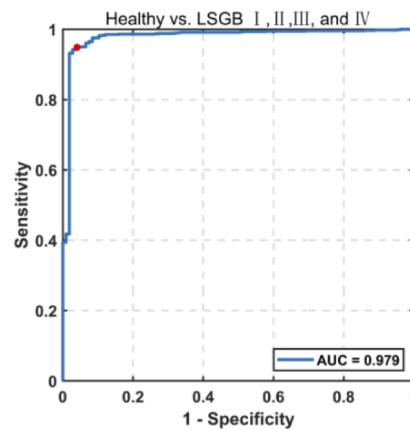


Fig. 7. ROC curve for distinguishing the healthy subjects from the rest (patients with LSGB I, II, III, and IV). The optimal threshold for the ROC was 0.949. At this threshold, sensitivity was 94.3%, specificity was 97.2%, AUC was 0.979.

Table 3. The accuracy of the training (left) and test (right) data sets for the four classifiers in each fold of cross-validation.

	Classifier 1	Classifier 2	Classifier 3	Classifier 4
1st fold	99.5, 97.3	100, 87.5	99.0, 88.5	99.1, 89.7
2nd fold	99.2, 98.4	99.9, 84.6	99.6, 89.4	99.4, 93.1
3rd fold	99.6, 98.9	100, 88.2	100, 87.7	99.1, 86.2
4th fold	99.5, 94.2	98.7, 86.5	99.8, 86.0	99.1, 88.4
5th fold	99.3, 97.4	99.0, 82.4	99.8, 87.0	99.4, 91.9

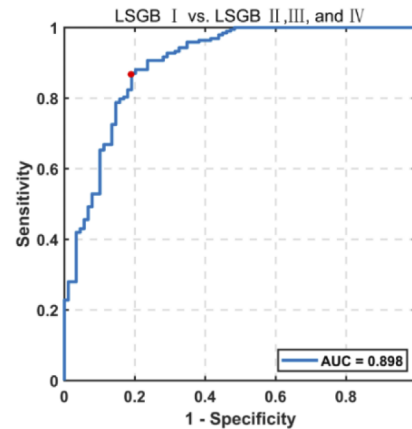


Fig. 8. ROC curve for distinguishing the patients with LSGB I from the rest (patients with LSGB II, III, and IV). The optimal threshold for the ROC was 0.647. At this threshold, sensitivity was 87.0%, specificity was 80.9%, AUC was 0.898.

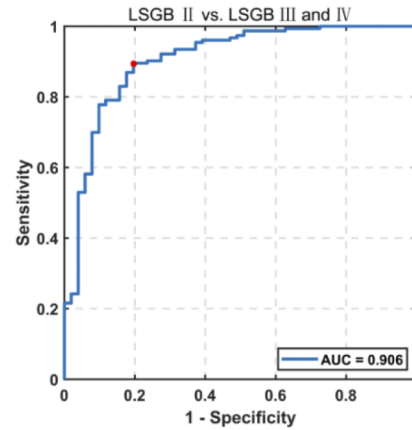


Fig. 9. ROC curve for distinguishing the patients with LSGB II from the rest (patients with LSGB III and IV). The optimal threshold for the ROC was 0.780. At this threshold, sensitivity was 89.5%, specificity was 80.4%, AUC was 0.906.

The data ($n = 1048$) was split 8:2 randomly into a training set and a test set. The features used in training include physiological parameters (THb, StO₂) and structural parameters (Alpha, h , μ'_{s1} , sp_1 , μ'_{s2} , sp_2). The parameters THb, StO₂, sp_1 , sp_2 , and the pair interaction sp_2 -THb were found to be the top 5 features contributing to the SS risk (see Fig. 11). The standard deviation is computed using the test set from six repeated experiments. Among these features, THb and StO₂ reflect the progress of SS affecting microcirculation, whereas sp_1 and sp_2 show the structural changes of the oral mucosal epithelium and lamina propria of SS patients. THb dominates among all risk factors.

Figure 12 shows the distribution of the risk score vs. the pathological grade in the test set in GAMI-Net analysis. The risk score becomes more elevated with the increasing pathological grade as expected.

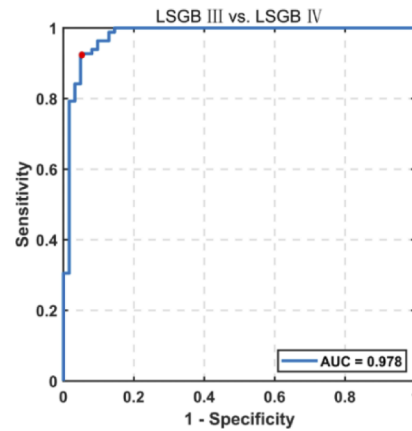


Fig. 10. ROC curve for distinguishing the patients with LSGB III from the patients with LSGB IV. The optimal threshold for the ROC was 0.662. At this threshold, sensitivity was 92.7%, specificity was 95.2%, AUC was 0.978.

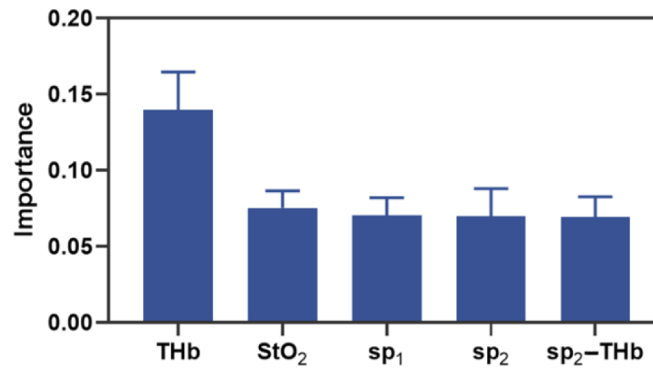


Fig. 11. Top 5 features contributing to SS risk.

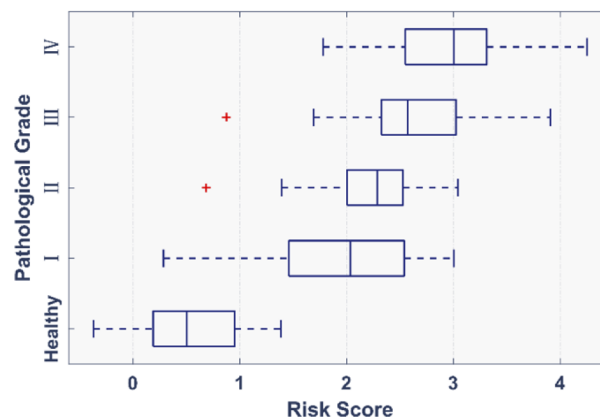


Fig. 12. The distribution of the risk score vs. the pathological grade. The vertical line in each box is a median (50th percentile) of the predicted risk score; the left and right sides of the box represent the 25th and 75th percentiles, respectively; and whiskers indicate the range from the largest to smallest risk score within a 1.5-interquartile range presented by the box.

4. Discussion

SS is an autoimmune disease, and regular check-ups and early diagnosis are essential for its control. Timely intervention can prevent serious long-term complications of the disease [38]. LSGB is a commonly performed procedure in diagnosing SS with critical implications in patient management. However, LSGB requires traumatic surgery and can cause morbidity to the patient.

The current study has successfully demonstrated an SSMD-SFDI imaging system for mapping the structural and hemodynamic properties of the layered oral mucosa label-free and performing an optical biopsy of SS. The rapid, noninvasive diagnosis brings convenience and comfort to doctors and patients. The portable device replaced the DMD used in our original design [13,43] with a grating to generate a sinusoidal pattern. An orthogonal saw-tooth pattern due to the grating's imperfection is evident in Fig. 3, representing high-frequency modulation superimposed on the desired low-frequency sinusoidal modulation. SSMD is capable of locking into the low spatial frequency modulation unaffected by the orthogonal modulation component [14]. Furthermore, we have compared the MTFs obtained for a pure sinusoidal modulation pattern and the same one superimposed by an orthogonal saw-tooth high-frequency modulation reflected by a reflection standard using DMD. The two cases produced identical MTFs for the sinusoidal modulation.

One unique strength of SFDI is the wide-field simultaneous imaging of absorption and scattering properties of a turbid medium [13,44]. We have selected an ROI within the imaging window for tissue characterization. The complete characterization of the ROI, including its structural and physiological parameters, provides a solid foundation for noninvasive Sjögren's syndrome labial salivary gland biopsy. Such characterization can not be obtained with point spectroscopy which mixes scattering and absorption effects.

Our proposed method accounts for the varying penetration depth of spatially modulated light at different modulation frequencies and wavelengths. The spatial frequency $f = 0.22\text{mm}^{-1}$ and three wavelengths were used, which offers excellent capability separating the two major chromophores (deoxyhemoglobin and oxyhemoglobin) in the oral mucosa with high sensitivity. Furthermore, the explicit consideration of oral mucosa's layered structure is critical in accurately quantifying its properties. Ignoring the two-layer structure, the parameters obtained by the homogeneous model tend to be erroneous [18]. For example, StO_2 predicted by the homogeneous model is underestimated (between 44% and 65%) and decreases as skin pigmentation increases. The two-layer model predicts realistic and similar values of StO_2 regardless of pigmentation, demonstrating the importance of accounting for the layered structure in the accurate recovery of hemoglobin concentration and oxygen saturation. The adopted strategy for mapping a layered medium to an equivalent homogeneous one has been successfully applied to image other layered structures, including cutaneous microcirculation under the reactive hyperemia protocol and diabetic foot [13,43].

The measured structural and physiological parameters of the oral mucosa are found to correlate significantly with SS progression. The SVM classifier distinguishes healthy, LSGB I, II, III, and IV subjects in sequence with AUCs of 0.979, 0.898, 0.906, and 0.978, respectively. The sensitivities of the four classifiers are 94.3%, 87.0%, 89.5%, and 92.7%, respectively, which are higher than the blood marker-antibody positivity method (anti-SS-A/SS-B alone) with the sensitivity of 74.9% [39]. Compared with other noninvasive methods such as parotid CT [40] and salivary gland ultrasound [41], the SSMD-SFDI imager has higher diagnostic accuracy for identifying SS. We note that a weighted SVM scheme with nested 5-fold cross-validation has been adopted to suppress potential biases and address the unbalanced data of limited size.

The risk factors for the progression of SS were further identified by an explainable neural network model GAMI-Net. The resulting risk score based on the measured parameters by the SSMD-SFDI imager provides a potential risk stratification indicator, useful for surveillance and treatment efficacy tracking of SS.

As a comparison, we further conducted principal component analysis (PCA) of the data set using SPSS 23.0. Three leading principal components (PC) were extracted with a cumulative variance contribution rate of 83.8%. The weights of all parameters are of the same order for PC1 (see Table 4), coinciding with the fact that the SVM classifier is optimal when all the features are selected. Additionally, StO₂ and THb are the leading factors according to the component matrix, consistent with the neural network analysis (see Fig. 11). Figure 13 compares the distribution of the three principal components for healthy subjects, patients with LSGB I, II, III, and IV. Among them, the principal component PC1 has the best discrimination power, in particular, in distinguishing between healthy subjects and patients with LSGB. However, no significant difference between LSGB I, II, III, and IV is observed for the three principal components. The risk score obtained through neural network analysis (see Fig. 12) is superior to PCA-based analysis in pathological classification (see Fig. 13).

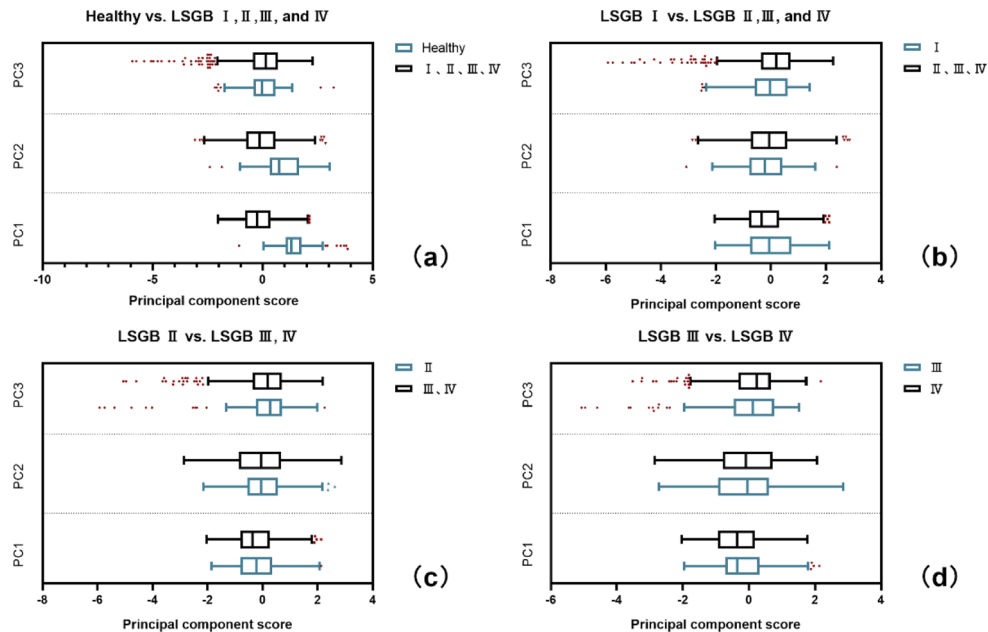


Fig. 13. The box plot shows the distribution of the three principal components (PC1, PC2, and PC3) in (a) Healthy vs. patients with LSGB I, II, III, and IV (b) patients with LSGB I vs. LSGB II, III, and IV (c) patients with LSGB II vs. LSGB III and IV (d) patients with LSGB III vs. LSGB IV.

The SS patients in this study have undergone LSGB. Biopsy findings identify SS at more advanced stages of disease when gland damage has already occurred [39]. Relevant studies have shown that patients with SS without a history of lung disease have a decrease in PaO₂ in lung function tests, with an average PaO₂ of 84 mmHg (the normal range of PaO₂ is 95-100 mmHg) [42]. This finding suggests local microcirculation disorders in the early stage of the disease (such as decreased StO₂) in the oral mucosa for SS patients. The SSMD-SFDI imager is hence potentially applicable to detect the early-stage SS.

The low-cost SSMD-SFDI imager thus presents a valuable label-free solution for early diagnosis, routine surveillance, and therapy monitoring of SS. Due to the rich structural and physiological information recoverable from SSMD-SFDI, our approach applies to noninvasive diagnosis, surveillance, and treatment efficacy tracking of many diseases affecting microcirculation and tissue structure in general [43].

Table 4. Component matrix.

	Component		
	1	2	3
THb	0.812	0.371	−0.197
StO ₂	0.812	0.349	0.189
μ'_{s1}	−0.798	0.516	0.075
sp ₁	−0.797	0.325	0.210
h	−0.668	0.676	0.024
Alpha	0.595	0.614	0.353
μ'_{s2}	0.483	0.436	−0.668
sp ₂	0.575	−0.067	0.629

5. Conclusion

In summary, we have presented a handheld SSMD-SFDI imager for imaging the oral mucosa and rapid optical biopsy of labial salivary gland label-free and noninvasively. The measured structural and physiological parameters of the epithelium and lamina propria correlate significantly with the progression of SS. An SVM classifier based on the measured parameters has been shown to distinguish healthy subjects, LSGB I, II, III, and IV patients in sequence with AUCs of 0.979, 0.898, 0.906, and 0.978, respectively in a pilot study. Critical structural and physiological alterations in the mucosa due to SS have been further identified and can serve as a potential SS risk stratification indicator based on an explainable neural network. The SSMD-SFDI imager will potentially replace LSGB with a noninvasive optical biopsy of the labial salivary gland. The handheld spatial frequency domain imager may emerge as a valuable label-free and versatile tool for early diagnosis, routine surveillance, and treatment efficacy monitoring of SS and other diseases.

Funding. Natural Science Foundation of Zhejiang Province (LGF18H180013, LQ18F05005, LZ16H180002); National Natural Science Foundation of China (61905181, 81470081); National Science Foundation (1607664); Wenzhou Municipal Science and Technology Bureau (ZS2017022).

Disclosures. The authors declare no financial or commercial conflict of interest. A patent has been filed for the optical labial salivary gland biopsy with the SSMD-SFDI imager.

Data availability. Data underlying the results presented in this paper are not publicly available at this time but may be obtained from the authors upon reasonable request.

References

1. R. I. Fox, "Sjögren's syndrome," *Lancet* **366**(9482), 321–331 (2005).
2. C. P. Mavragani and H. M. Moutsopoulos, "The geoepidemiology of Sjögren's syndrome," *Autoimmun. Rev.* **9**(5), A305–A310 (2010).
3. M. Margaix-Munoz, J. V. Bagan, R. Poveda, Y. Jimenez, and G. Sarrion, "Sjogren's syndrome of the oral cavity: review and update," *Med. Oral Patol. Oral Cir. Bucal.* **14**(7), E325–E330 (2009).
4. R. Seror, S. J. Bowman, P. Brito-Zeron, E. Theander, H. Bootsma, A. Tzioufas, J. E. Gottenberg, M. Ramos-Casals, T. Dorner, P. Ravaut, C. Vitali, X. Mariette, K. Asmussen, S. Jacobsen, E. Bartoloni, R. Gerli, J. W. Bijlsma, A. A. Kruize, S. Bombardieri, A. Bookman, C. Kallenberg, P. Meiners, J. G. Brun, R. Jonsson, R. Caporali, S. Carsons, S. De Vita, N. Del Papa, V. Devauchelle, A. Saraux, A. L. Fauchais, J. Sibilia, E. Hachulla, G. Illei, D. Isenberg, A. Jones, M. Manoussakis, T. Mandl, L. Jacobsson, F. Demoulin, C. Montecucco, W. F. Ng, S. Nishiyama, R. Omdal, A. Parke, S. Praprotnik, M. Tomsic, E. Price, H. Scofield, L. S. K. J. Smolen, R. S. Laque, S. Steinfeld, N. Sutcliffe, T. Sumida, G. Valesini, V. Valim, F. B. Vivino, and C. Vollenweider, "EULAR Sjogren's syndrome disease activity index (ESSDAI): a user guide," *RMD Open* **1**(1), e000022 (2015).
5. C. P. Mavragani and H. M. Moutsopoulos, "Sjogren syndrome," *Can. Med. Assoc. J.* **186**(15), E579–E586 (2014).
6. C. Vitali, S. Bombardieri, R. Jonsson, H. M. Moutsopoulos, E. L. Alexander, S. E. Carsons, T. E. Daniels, P. C. Fox, R. I. Fox, S. S. Kassan, S. R. Pillemer, N. Talal, and M. H. Weisman, and S. European Study Group on Classification Criteria for Sjogren's, "Classification criteria for Sjogren's syndrome: a revised version of the European criteria proposed by the American-European Consensus Group," *Ann. Rheum. Dis.* **61**(6), 554–558 (2002).

7. S. C. Shiboski, C. H. Shiboski, L. Criswell, A. Baer, S. Challacombe, H. Lanfranchi, M. Schiodt, H. Umehara, F. Vivino, Y. Zhao, Y. Dong, D. Greenspan, A. M. Heidenreich, P. Helin, B. Kirkham, K. Kitagawa, G. Larkin, M. Li, T. Lietman, J. Lindegaard, N. McNamara, K. Sack, P. Shirlaw, S. Sugai, C. Vollenweider, J. Whitcher, A. Wu, S. Zhang, W. Zhang, J. Greenspan, and T. Daniels, and G. Sjogren's International Collaborative Clinical Alliance Research, "American College of Rheumatology classification criteria for Sjogren's syndrome: a data-driven, expert consensus approach in the Sjogren's International Collaborative Clinical Alliance cohort," *Arthritis. Care Res.* **64**(4), 475–487 (2012).
8. C. H. Shiboski, S. C. Shiboski, R. Seror, L. A. Criswell, M. Labetoulle, T. M. Lietman, A. Rasmussen, H. Scofield, C. Vitali, S. J. Bowman, and X. Mariette, and G. International Sjogren's Syndrome Criteria Working, "2016 American College of Rheumatology/European League Against Rheumatism classification criteria for primary Sjogren's syndrome: A consensus and data-driven methodology involving three international patient cohorts," *Ann. Rheum. Dis.* **76**(1), 9–16 (2017).
9. A. J. Niikura, S. Yamachika, K. Yamamoto, M. R. Okamoto, Y. F. Ikeda, S. Nakamura, E. Oda, T. K. Imamura, I. Saito, and Y. Nakagawa, "Efficient diagnosis of Sjogren's syndrome to reduce the burden on patients," *Mod. Rheumatol.* **25**(1), 100–104 (2015).
10. D. Guellec, D. Cornec, S. Jousse-Joulin, T. Marhadour, P. Marcorelles, J. O. Pers, A. Saraux, and V. Devauchelle-Pensec, "Diagnostic value of labial minor salivary gland biopsy for Sjogren's syndrome: a systematic review," *Autoimmun. Rev.* **12**(3), 416–420 (2013).
11. J. Kim, D. Sun, R. Ozl, T. Grader-Beck, J. Birnbaum, E. K. Akpek, and A. N. Baer, "A validated method of labial minor salivary gland biopsy for the diagnosis of Sjogren's syndrome," *Laryngoscope* **126**(9), 2041–2046 (2016).
12. R. A. Giovelli, M. C. Santos, E. V. Serrano, and V. Valim, "Clinical characteristics and biopsy accuracy in suspected cases of Sjogren's syndrome referred to labial salivary gland biopsy," *BMC Musculoskeletal Disord.* **16**(1), 30 (2015).
13. X. Chen, W. Lin, C. Wang, S. Chen, J. Sheng, B. Zeng, and M. Xu, "In vivo realtime imaging of cutaneous hemoglobin concentration, oxygen saturation, scattering properties, melanin content, and epidermal thickness with visible spatially modulated light," *Biomed. Opt. Express* **8**(12), 5468–5482 (2017).
14. M. Xu, Z. Cao, W. Lin, X. Chen, L. Zheng, and B. Zeng, "Single snapshot multiple frequency modulated imaging of subsurface optical properties of turbid media with structured light," *AIP Adv.* **6**(12), 125208 (2016).
15. Z. Cao, W. Lin, X. Chen, B. Zeng, and X. Min, "Realtime spatial frequency domain imaging by single snapshot multiple frequency demodulation technique," *Spie Bios* **10059**, 100590Z (2017).
16. M. Xu, "Low-coherence enhanced backscattering beyond diffusion," *Opt. Lett.* **33**(11), 1246–1248 (2008).
17. M. Xu, "Diagnosis of the phase function of random media from light reflectance," *Sci. Rep.* **6**(1), 22535 (2016).
18. D. Yudovsky, J. Q. Nguyen, and A. J. Durkin, "In vivo spatial frequency domain spectroscopy of two layer media," *J. Biomed. Opt.* **17**(10), 107006 (2012).
19. R. B. Saager, A. Truong, D. J. Cuccia, and A. J. Durkin, "Method for depth-resolved quantitation of optical properties in layered media using spatially modulated quantitative spectroscopy," *J. Biomed. Opt.* **16**(7), 077002 (2011).
20. A. T. Cruchley and L. A. Bergmeier, *Structure and Functions of the Oral Mucosa*, L. A. Bergmeier, ed. (Springer, 2018), pp. 1–18.
21. M. Xu, "Plum pudding random medium model of biological tissue toward remote microscopy from spectroscopic light scattering," *Biomed. Opt. Express* **8**(6), 2879–2895 (2017).
22. T. T. Wu, J. Y. Qu, and M. Xu, "Unified Mie and fractal scattering by biological cells and subcellular structures," *Opt. Lett.* **32**(16), 2324–2326 (2007).
23. M. Xu, T. T. Wu, and J. Y. Qu, "Unified Mie and fractal scattering by cells and experimental study on application in optical characterization of cellular and subcellular structures," *J. Biomed. Opt.* **13**(2), 024015 (2008).
24. M. Xu and R. R. Alfano, "Fractal mechanisms of light scattering in biological tissue and cells," *Opt. Lett.* **30**(22), 3051–3053 (2005).
25. D. M. Chisholm and D. K. Mason, "Labial salivary gland biopsy in Sjogren's disease," *J. Clin. Pathol.* **21**(5), 656–660 (1968).
26. M. Ramos-Casals, J. Font, M. Garcia-Carrasco, M. P. Brito, J. Rosas, J. Calvo-Alen, L. Pallares, R. Cervera, and M. Ingelmo, "Primary Sjogren syndrome: hematologic patterns of disease expression," *Medicine* **81**(4), 281–292 (2002).
27. T. L. Moore and A. M. Dalrymple, "Laboratory studies in autoimmune diseases," *Mo. Med.* **113**(2), 118–122 (2016).
28. I. Ito, S. Nagai, M. Kitaichi, A. G. Nicholson, T. Johkoh, S. Noma, D. S. Kim, T. Handa, T. Izumi, and M. Mishima, "Pulmonary manifestations of primary Sjogren's syndrome: a clinical, radiologic, and pathologic study," *Am. J. Respir. Crit. Care Med.* **171**(6), 632–638 (2005).
29. S. A. Mathews, B. T. Kuriem, and R. H. Scofield, "Oral manifestations of Sjogren's syndrome," *J. Dent. Res.* **87**(4), 308–318 (2008).
30. S. Prestin, S. I. Rothschild, C. S. Betz, and M. Kraft, "Measurement of epithelial thickness within the oral cavity using optical coherence tomography," *Head Neck* **34**(12), 1777–1781 (2012).
31. I. Grulkowski, J. K. Nowak, K. Karnowski, P. Zebryk, M. Puszczewicz, J. Walkowiak, and M. Wojtkowski, "Quantitative assessment of oral mucosa and labial minor salivary glands in patients with Sjogren's syndrome using swept source OCT," *Biomed. Opt. Express* **5**(1), 259–274 (2014).
32. T. Yatagai, Y. Aizu, O. Matoba, Y. Awatsuji, C.-Y. Lee, W.-C. Chen, and M.-T. Tsai, "Noninvasive imaging of oral mucosae with optical coherence tomography," *Proc. SPIE* **10251**, 102511E (2017).

33. B. Busamia, C. Gobbi, E. Albiero, and M. Yorio, "Assessment of cytology techniques in oral mucosa of Sjögren's syndrome patients," *Revista Odontológica Mexicana* **22**(1), 29–33 (2018).
34. G. A. Scardina, A. Ruggieri, and P. Messina, "Evaluation of labial microvessels in Sjogren syndrome: a videocapillaroscopic study," *Ann. Anat.* **191**(3), 273–279 (2009).
35. C. C. Chang and C. J. Lin, "LIBSVM: A library for support vector machines," *ACM Trans. Intell. Syst. Technol.* **2**(3), 1–27 (2011).
36. E. Hernandez-Lemus, A. Vabalas, E. Gowen, E. Poliakoff, and A. J. Casson, "Machine learning algorithm validation with a limited sample size," *PLoS One* **14**(11), e0224365 (2019).
37. Z. Yang, A. Zhang, and A. Sudjianto, "GAMI-Net: an explainable neural network based on generalized additive models with structured interactions," arXiv:2003.07132 (2020).
38. S. M. Amin, Y. E. Taha, H. Samir, B. C. Khalifa, and T. O. Fawzy, "Sjogren syndrome with nasal dryness: an ultrastructural study of nasal mucosa," *Med. J. Cairo Univ.* **79**(1), 73–79 (2011).
39. K. A. Beckman, J. Luchs, M. S. Milner, and J. L. Ambrus, "The potential role for early biomarker testing as part of a modern, multidisciplinary approach to Sjögren's syndrome diagnosis," *Adv. Ther.* **34**(4), 799–812 (2017).
40. Z. Sun, Z. Zhang, K. Fu, Y. Zhao, D. Liu, and X. Ma, "Diagnostic accuracy of parotid CT for identifying Sjogren's syndrome," *Eur. J. Radiol.* **81**(10), 2702–2709 (2012).
41. M. Zhou, S. Song, S. Wu, T. Duan, L. Chen, J. Ye, and J. Xiao, "Diagnostic accuracy of salivary gland ultrasonography with different scoring systems in Sjogren's syndrome: a systematic review and meta-analysis," *Sci. Rep.* **8**(1), 17128 (2018).
42. S. A. Papiris, M. Maniati, S. H. Constantopoulos, C. Roussos, H. M. Moutsopoulos, and F. N. Skopouli, "Lung involvement in primary Sjögren's syndrome is mainly related to the small airway disease," *Ann. Rheum. Dis.* **58**(1), 61–64 (1999).
43. Y. Li, M. Guo, X. Qian, W. Lin, Y. Zheng, K. Yu, B. Zeng, Z. Xu, C. Zheng, and M. Xu, "Single snapshot spatial frequency domain imaging for risk stratification of diabetes and diabetic foot," *Biomed. Opt. Express* **11**(8), 4471–4483 (2020).
44. W. Lin, B. Zeng, Z. Cao, X. Chen, K. Yang, and M. Xu, "Quantitative diagnosis of tissue microstructure with wide-field high spatial frequency domain imaging," *Biomed. Opt. Express* **9**(7), 4471–4483 (2018).